

OFTSR: One-Step Flow for Image Super-Resolution with Tunable Fidelity-Realism Trade-offs

Yuanzhi Zhu^{1,2,*} Ruiqing Wang¹ Shilin Lu³ Junnan Li² Hanshu Yan² Kai Zhang^{1,†}
¹Nanjing University ²Rhymes.AI ³Nanyang Technological University

Abstract

Recent advances in diffusion and flow-based generative models have demonstrated remarkable success in image restoration tasks, achieving superior perceptual quality compared to traditional deep learning approaches. However, these methods either require numerous sampling steps to generate high-quality images, resulting in significant computational overhead, or rely on model distillation, which usually imposes a fixed fidelity-realism trade-off and thus lacks flexibility. In this paper, we introduce OFTSR, a novel flow-based framework for one-step image super-resolution that can produce outputs with tunable levels of fidelity and realism. Our approach first trains a conditional flow-based super-resolution model to serve as a teacher model. We then distill this teacher model by applying a specialized constraint. Specifically, we force the predictions from our one-step student model for same input to lie on the same sampling ODE trajectory of the teacher model. This alignment ensures that the student model’s single-step predictions from initial states match the teacher’s predictions from a closer intermediate state. Through extensive experiments on challenging datasets including FFHQ (256×256), DIV2K, and ImageNet (256×256), we demonstrate that OFTSR achieves state-of-the-art performance for one-step image super-resolution, while having the ability to flexibly tune the fidelity-realism trade-off. Code and pre-trained models are available at <https://github.com/yuanzhi-zhu/OFTSR> and <https://huggingface.co/Yuanzhi/OFTSR>, respectively.

1. Introduction

Recently, diffusion and flow-based generative models have demonstrated the ability to generate images with higher quality [13, 40, 43] than earlier generative models such as Generative Adversarial Networks (GANs) [16, 21], Normalizing Flows (NFs) [14] and Variational Autoencoders

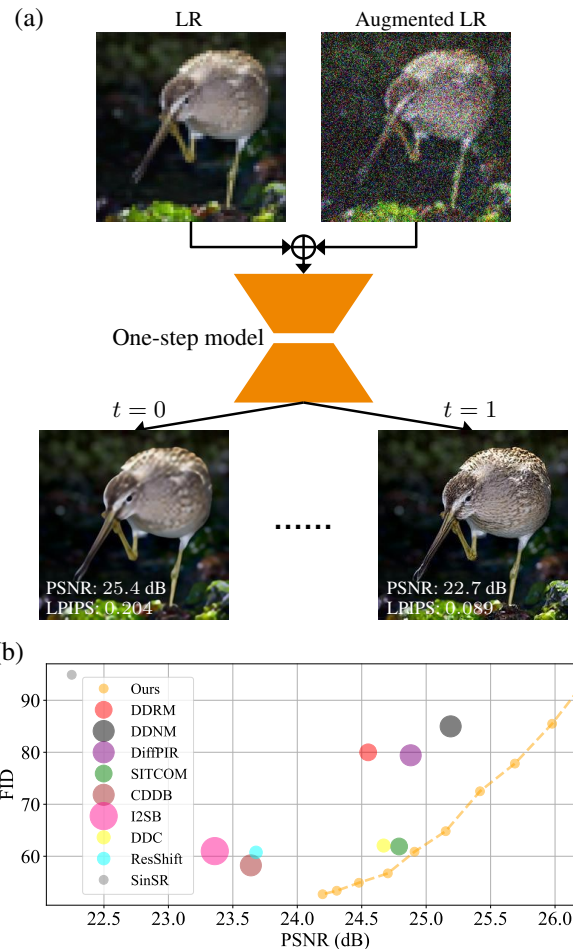


Figure 1. (a) Our final model takes the concatenation of a low-resolution image with its noise-augmented version as input, and is able to generate high-resolution outputs with either high realism or high fidelity by adjusting the interpolation parameter t . We indicate the PSNR and LPIPS value on the output images. (b) Comparison of different diffusion and flow based image super-resolution methods on the ImageNet 256 × 256 dataset. Bubble radius indicates the NFEs used by the methods.

*Work done while interned at Rhymes.AI (zyzeroer@gmail.com)

†Corresponding author (kaizhang@nju.edu.cn)

(VAEs) [25, 44]. Beyond visual generation, diffusion models have shown remarkable success across a variety of tasks, including image editing [5, 18, 23], 3D content generation [33, 42, 58, 59, 65], and image restoration [9, 11, 22, 28, 62, 76], with particularly notable advancements in image super-resolution (SR) [7, 47, 60, 74].

The degradation model for image SR problems can be typically written as:

$$\mathbf{y} = \mathcal{H}(\mathbf{x}) + \mathbf{n}, \quad (1)$$

where \mathbf{x} and \mathbf{y} correspond to High-Resolution (HR) and Low-Resolution (LR) images, respectively, and \mathbf{n} denotes i.i.d. Gaussian noise with standard deviation σ_n . The down-scaling operator and its transpose are represented by \mathcal{H} and \mathcal{H}^T , respectively. Given the ill-posed nature of SR, multiple plausible HR reconstructions from the conditional distribution $p(\mathbf{x}|\mathbf{y})$ can correspond to a single LR input \mathbf{y} . This highlights the inherent uncertainty and ambiguity in recovering HR details from LR observations.

Existing diffusion and flow-based SR methods can be broadly divided into two approaches: training-free methods [2, 9, 22, 38, 52, 62, 76], and training-based methods [11, 30, 31, 37, 47, 63, 72, 74]. Training-free methods decompose the conditional probability into a prior term and a likelihood term, with each term associating directly to a specific subproblem [76]. During iterative sampling, the prior subproblem is naturally handled by pre-trained unconditional diffusion models, which serve as powerful regularizers to guide the solution toward realistic HR images. Meanwhile, the likelihood subproblem is addressed through specialized optimization techniques or analytical approximations to ensure fidelity to the observed LR image. On the other hand, training-based methods directly model the conditional probability using paired data, either by training from scratch [11, 47] or by incorporating additional control modules [28, 60, 71] into existing generative priors [45]. Several other bridge-based methods [10, 30, 37, 72] have also been proposed for general image-to-image translation tasks, sharing similarities with direct learning approaches.

Despite the promising results of above methods, they require many iterative sampling steps to achieve high perceptual quality, and reducing the number of iterations often results in higher fidelity but lower perceptual quality. In this sense, their fidelity-realism trade-offs can be controlled by adjusting the number of sampling steps. In order to achieve high perceptual quality with fewer sampling steps, some attempts [26, 27, 63, 66, 67] have been made to distill the diffusion sampling process into a single step with diffusion distillation approaches [34, 35, 49, 50, 56, 68–70]. However, these approaches sacrifice the ability to produce outputs with flexible trade-offs between fidelity and realism, leading to limited applicability [39].

In this paper, we propose OFTSR that achieves one-

step image SR and preserves the capability to produce outputs with tunable fidelity-realism trade-offs. Specifically, OFTSR adopts a two-stage training pipeline. In the first stage, a simple conditional rectified flow training strategy is introduced to learn the conditional probability directly. It uses noise-augmented LR images to form the initial distribution and LR images as conditions. In the second stage, a distillation strategy is proposed to restrict the student model’s predictions to match the same Ordinary Differential Equation (ODE) induced by the teacher model from the first stage. We conduct extensive experiments on diverse datasets to evaluate OFTSR, including DIV2K [1], FFHQ 256×256 [21], and ImageNet 256×256 [12]. OFTSR achieves competitive one-step reconstruction metrics in comparison to other recent methods.

2. Background

2.1. Diffusion and Flow-Based Generative Models

Drawing inspiration from non-equilibrium thermodynamics, diffusion models operate through two core processes: a forward diffusion process that gradually adds Gaussian noise to data until it becomes pure noise, and a reverse denoising process that systematically reconstructs the original data by removing noise [19, 51, 55]. Let \mathbf{x}_t represent the data \mathbf{x} at timestep t . The forward process can be formally described by the Itô Stochastic Differential Equation (SDE) [55]:

$$d\mathbf{x}_t = f_t \mathbf{x}_t dt + g_t d\mathbf{w}, \quad (2)$$

where \mathbf{w} is the standard Wiener process, $f_t : \mathbb{R} \rightarrow \mathbb{R}$ is the drift coefficient, and $g_t : \mathbb{R} \rightarrow \mathbb{R}$ is a scalar function called the diffusion coefficient.

For every diffusion process described by Eq. (2), there exists a corresponding deterministic Probability Flow Ordinary Differential Equation (PF-ODE) that maintains the same marginal probability density:

$$\frac{d\mathbf{x}_t}{dt} = f_t \mathbf{x}_t - \frac{1}{2} g_t^2 \nabla_{\mathbf{x}_t} \log p_t(\mathbf{x}_t), \quad (3)$$

where $p_t(\cdot)$ represents the marginal probability density at time t . The term $\nabla_{\mathbf{x}_t} \log p_t(\mathbf{x}_t)$ is known as the score function, which can be approximated by a neural network $\mathbf{s}_\theta(\mathbf{x}, t)$ with parameters θ . This network is typically trained using score matching techniques [20, 53, 54].

To generate data samples, the process begins with Gaussian noise drawn from an initial Gaussian distribution p_0 and solves Eq. (3) numerically from $t = 0$ to $t = 1$. By utilizing the learned score function $\mathbf{s}_\theta(\mathbf{x}_t, t)$, the empirical PF-ODE can be obtained as: $\frac{d\mathbf{x}_t}{dt} = f_t \mathbf{x}_t - \frac{1}{2} g_t^2 \mathbf{s}_\theta(\mathbf{x}_t, t)$.

Rectified flow [15, 29, 32, 34] is a generative modeling framework based on ODEs. Given an initial distribution p_0 and a target data distribution p_1 , rectified flow trains a neural

network to parameterize a velocity field using the following loss function:

$$\mathcal{L}_{\text{rf}}(\theta) := \mathbb{E}_{\mathbf{x}_1 \sim p_1, \mathbf{x}_0 \sim p_0} \left[\int_0^1 \left\| \mathbf{v}_\theta(\mathbf{x}_t, t) - (\mathbf{x}_1 - \mathbf{x}_0) \right\|_2^2 dt \right],$$

where $\mathbf{x}_t = (1-t)\mathbf{x}_0 + t\mathbf{x}_1$.

(4)

Once trained, sample generation is achieved by solving the following ODE from $t = 0$ to $t = 1$:

$$\frac{d\mathbf{x}_t}{dt} = \mathbf{v}_\theta(\mathbf{x}_t, t).$$
(5)

In practical implementations, Eq. (5) is solved numerically using standard ODE solvers, ranging from the simple forward Euler method to higher-order methods such as RK2 and RK45.

2.2. Perception-distortion Trade-off

The perception-distortion (realism-fidelity) trade-off [4] is a fundamental concept in image restoration. It describes the inherent trade-off between perceptual realism and fidelity to the ground truth and mathematically proves that it is generally not possible to achieve both good perceptual realism and high fidelity simultaneously.

To address this challenge, researchers have explored various approaches to enable tunable trade-offs between these two desirable qualities. One common technique involves interpolating between the weights of two models with the same architecture and trained using GAN loss and mean squared error loss [61]. More recently, diffusion models have emerged as a promising approach for this task. The iterative sampling nature of diffusion models provides a flexible means of controlling the desired trade-offs. By adjusting the Number of Function Evaluations (NFEs), users can generate reconstructions that better match their specific requirements [10]. Specifically, lower NFEs values tend to result in reconstructions with reduced distortion, as the output regresses towards the mean [11]. Conversely, higher NFEs values prioritize perceptual quality, even if it comes at the expense of some distortion from the ground truth (similar to Fig. 3).

3. Method

In this section, we introduce the OFTSR framework for one-step SR models that can restore HR images with either high realism or high fidelity. We achieve this goal through a two-stage process: first, we train a direct flow-based model for SR, and then we distill this learned model into a simplified one-step variant. In Sec. 3.1, we present a simple conditional flow training strategy that uses noise-augmented LR images as the initial distribution and LR images as conditions. In Sec. 3.2, we propose to distill the student model

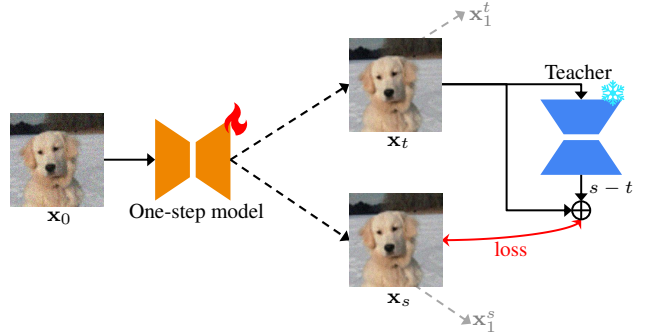


Figure 2. Illustration of the proposed distillation loss. Rather than directly distilling from the teacher, we leverage the teacher model to align the one-step pseudo outputs, \mathbf{x}_t and \mathbf{x}_s , along the same PF-ODE trajectory. For simplicity, LR conditioning is omitted in this figure.

by restricting its predictions on the same ODE using teacher model from Sec. 3.1.

3.1. Noise Augmented Conditional Flow

Unlike diffusion models, flow-based models have the advantage that their initial distribution is not limited to Gaussian distributions. This flexibility suggests a natural approach for image restoration - directly learning a flow that maps the distribution of LR images (p_{LR}) to that of HR images (p_{HR}). However, our initial experiments (see Tab. 4) showed poor performance with this direct approach, aligning with findings from several recent works [11, 24, 26].

As suggested by [24] and further demonstrated in [11, 37], the solution lies in augmenting the input with Gaussian noise. This noise augmentation expands the support of the initial distribution and ensures the ODE mapping from p_0 to $p_1 = p_{\text{HR}}$ is well-defined [24].

Based on these insights, we adopt a noise-augmented approach to process LR images. For any input image \mathbf{x}_{LR} , we construct our initial distribution $p_0(\mathbf{x}) = p_{\text{LR}}^{\sigma_p}$ by adding Gaussian noise with standard deviation σ_p . Specifically, we use a Variance-Preserving (VP) noising process [19, 55]:

$$\mathbf{x}_0 = \sqrt{1 - \sigma_p^2} \mathbf{x}_{\text{LR}} + \sigma_p \epsilon, \quad (6)$$

where ϵ is a standard Gaussian noise. While this noise perturbation facilitates better generalization, it inevitably causes information loss in the LR image. To address this, we incorporate \mathbf{x}_{LR} as a conditional input to our model as in Fig. 1a. This VP formulation, together with the condition \mathbf{x}_{LR} , makes our method particularly versatile, encompassing previous approaches as special cases. When $\sigma_p = 0$, our method reduces to the minimal augmentation case in InDI [11], and when $\sigma_p = 1$, it matches the training strategy of SR3 [48].

Given this noise-augmented formulation, we can now

define our training objective as:

$$\mathcal{L}_{\text{flow}}(\theta) = \mathbb{E}_{\mathbf{x}_1 \sim p_1} \left[\int_0^1 \mathbb{D} \left(\mathbf{v}_\theta(\mathbf{x}_{t,\text{LR}}, t), (\mathbf{x}_1 - \mathbf{x}_0) \right) dt \right], \quad (7)$$

where \mathbb{D} is a discrepancy loss that measures the difference between two images (e.g., ℓ_2 loss or the ℓ_1 loss), \mathbf{v}_θ is our velocity model, $\mathbf{x}_{t,\text{LR}} = \text{concat}(\mathbf{x}_t, \mathbf{x}_{\text{LR}})$ is the concatenation \mathbf{x}_t and \mathbf{x}_{LR} in channel dimension (see Fig. 1a), $\mathbf{x}_{\text{LR}} = \mathcal{H}^T(\mathcal{H}(\mathbf{x}_1) + \mathbf{n})$ represents the LR input of the training algorithm, and \mathbf{x}_0 is a perturbed version of \mathbf{x}_{LR} following the noise augmentation strategy in Eq. (6). Additionally, $\mathbf{x}_t = (1-t)\mathbf{x}_0 + t\mathbf{x}_1$ denotes the intermediate state as in rectified flow [32, 34].

3.2. Distillation Loss

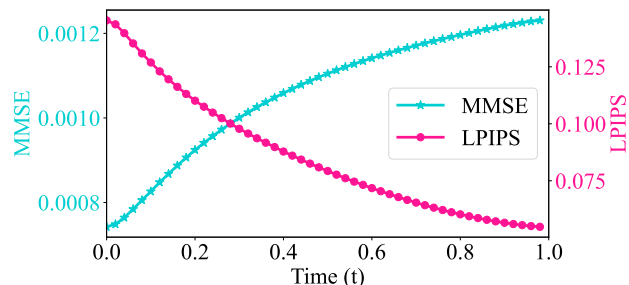


Figure 3. Metrics evaluation of estimated \mathbf{x}_1^t across different timesteps t . During sampling, at each timestep t , we estimate the final image \mathbf{x}_1^t using the current model prediction $\mathbf{v}_\theta(\mathbf{x}_{t,\text{LR}}, t)$ and state \mathbf{x}_t via $\mathbf{x}_1^t = \mathbf{x}_t + (1-t)\mathbf{v}_\theta(\mathbf{x}_{t,\text{LR}}, t)$. Both MMSE and LPIPS metrics are averaged over 100 sampling processes. We present MMSE instead of PSNR for better visual effect.

Once our model is trained using the objective in Eq. (7), we can roughly estimate the final state \mathbf{x}_1^t from any intermediate state \mathbf{x}_t with single step model evaluation. As demonstrated in Fig. 3, and presented in many previous works [11, 30], there exists a trade-off in these estimations: states closer to $t = 1$ exhibit richer details and lower LPIPS scores, while states closer to $t = 0$ produce more blurry results but achieve lower MMSE (higher PSNR) scores.

Based on this observation, our aim is to distill our teacher flow \mathbf{v}_θ into a student model \mathbf{v}_ϕ . The student model should preserve the teacher’s capabilities while offering a key advantage: the ability to achieve any desired point along this quality trade-off curve in a single step, controlled by a single hyperparameter t .

Similar to the teacher model, our one-step student model \mathbf{v}_ϕ takes \mathbf{x}_0 , \mathbf{x}_{LR} , and t as input, and directly outputs the image \mathbf{x}_1^t according to:

$$\mathbf{x}_1^t = \mathbf{x}_0 + \mathbf{v}_\phi(\mathbf{x}_0, \mathbf{x}_{\text{LR}}, t), \quad (8)$$

where $\mathbf{x}_{0,\text{LR}} = \text{concat}(\mathbf{x}_0, \mathbf{x}_{\text{LR}})$ is the concatenation of the

input image \mathbf{x}_0 and the LR condition \mathbf{x}_{LR} along the channel dimension.

While the one-step model directly outputs \mathbf{x}_1^t , we can also compute the intermediate image \mathbf{x}_t at the input timestep t using:

$$\mathbf{x}_t = \mathbf{x}_0 + t\mathbf{v}_\phi(\mathbf{x}_{0,\text{LR}}, t). \quad (9)$$

For the same input $\mathbf{x}_{0,\text{LR}}$ and two different timesteps t and s where $s > t$, we want the corresponding intermediate images \mathbf{x}_t and \mathbf{x}_s from the student model to be on the same ODE trajectory described by the teacher model. In other words, as demonstrated in Fig. 2, we want the following relationship to be satisfied:

$$\mathbf{x}_s = \mathbf{x}_t + (s-t)\mathbf{v}_\theta(\mathbf{x}_{t,\text{LR}}, t). \quad (10)$$

It is important to note that Eqs. (9) and (10) together provide a stronger, but not necessary, condition to ensure the one-step generation capability of the student model. This property does not apply to other one-step SR methods like those described in [26, 63].

Substituting the expression for the intermediate image \mathbf{x}_t and \mathbf{x}_s from Eq. (9) into Eq. (10), we have the following constraint on the student model:

$$\begin{aligned} & s(\mathbf{v}_\phi(\mathbf{x}_{0,\text{LR}}, s) - \mathbf{v}_\phi(\mathbf{x}_{0,\text{LR}}, t)) \\ &= (s-t)(\mathbf{v}_\theta(\mathbf{x}_{t,\text{LR}}, t) - \mathbf{v}_\phi(\mathbf{x}_{0,\text{LR}}, t)). \end{aligned} \quad (11)$$

Similar to BOOT, we can set $dt = s - t$ and derive the final distillation loss:

$$\begin{aligned} \mathcal{L}_{\text{distill}}(\phi) = & \mathbb{E}_{\mathbf{x}_1 \sim p_1, t \sim \mathcal{U}[0,1]} \left[\left\| \mathbf{v}_\phi(\mathbf{x}_{0,\text{LR}}, s) - \right. \right. \\ & \left. \left. \text{SG} \left[\mathbf{v}_\phi(\mathbf{x}_{0,\text{LR}}, t) + \frac{dt}{s} (\mathbf{v}_\theta(\mathbf{x}_{t,\text{LR}}, t) - \mathbf{v}_\phi(\mathbf{x}_{0,\text{LR}}, t)) \right] \right\|_2^2 \right], \end{aligned} \quad (12)$$

where $\text{SG}[\cdot]$ is the stop-gradient operator for training stability [17, 57]. Since $s - t = dt$ and $t > 0$, we do not have the ‘dividing by 0’ issue in [57]. Similarly to [17, 56], we can use the Euler or general RK2 solver to calculate \mathbf{v}_θ in Eq. (12). In our main experiments, we employ the midpoint method, while also evaluating two other RK2 solver variants, *i.e.*, Heun’s method and Ralston’s method, for comparison in our ablations (see Tab. 5).

3.3. Alignment and Boundary Loss

In BOOT [17], a boundary condition is applied to enforce that the one-step student model and teacher model perform the same at the boundary $t = 0$. We aim to align the teacher and student outputs in our model. The student produces $\mathbf{x}_0 + \mathbf{v}_\phi(\mathbf{x}_{0,\text{LR}}, 0)$, while the teacher generates $\mathbf{x}_t + (1-t)\mathbf{v}_\theta(\mathbf{x}_{t,\text{LR}}, t)$ based on the student’s output using Eq. (9). By minimizing the difference between these

outputs, we get the following alignment loss to align the teacher and student:

$$\mathcal{L}_{\text{align}}(\phi) = \mathbb{E}_{\mathbf{x}_1 \sim p_1, t \sim \mathcal{U}[0,1]} \left[\left\| (1-t) \left(\mathbf{v}_\phi(\mathbf{x}_{0,\text{LR}}, t) - \mathbf{v}_\theta(\mathbf{x}_{t,\text{LR}}, t) \right) \right\|_2^2 \right]. \quad (13)$$

If we consider this alignment loss only at $t = 0$, it becomes equivalent to the boundary loss used in BOOT:

$$\mathcal{L}_{\text{BC}}(\phi) = \mathbb{E}_{\mathbf{x}_1 \sim p_1} \left[\left\| \mathbf{v}_\phi(\mathbf{x}_{0,\text{LR}}, 0) - \mathbf{v}_\theta(\mathbf{x}_{0,\text{LR}}, 0) \right\|_2^2 \right]. \quad (14)$$

Since it is difficult to sample $t = 0$ for most training iterations, we can keep the boundary loss Eq. (14) in our final training objective.

The overall training objective. The student network \mathbf{v}_ϕ is trained to minimize the combination of the aforementioned three losses terms:

$$\mathcal{L}(\phi) = \mathcal{L}_{\text{distill}}(\phi) + \lambda_{\text{align}} \mathcal{L}_{\text{align}}(\phi) + \lambda_{\text{BC}} \mathcal{L}_{\text{BC}}(\phi), \quad (15)$$

where λ_{align} and λ_{BC} are the weights for alignment loss and boundary condition loss, respectively. The distillation stage of the proposed method is summarized in Algorithm 1.

Algorithm 1 OFTSR Distillation

- Require:** teacher flow \mathbf{v}_θ , dataset \mathcal{D}_{HR} , σ_n , σ_p , dt , $w(t)$
- 1: Initialize the one-step student \mathbf{v}_ϕ with the weights of \mathbf{v}_θ
 - 2: **repeat**
 - 3: Randomly sample $\mathbf{x}_1 \sim \mathcal{D}_{\text{HR}}$; $t \sim \mathcal{U}[0, 1]$
 - 4: Randomly sample $\mathbf{n} \sim \mathcal{N}(\mathbf{0}, \sigma_n \mathbf{I})$; $\mathbf{n}_p \sim \mathcal{N}(\mathbf{0}, \sigma_p \mathbf{I})$
 - 5: Compute $\mathbf{x}_{\text{LR}} = \mathcal{H}^T(\mathcal{H}(\mathbf{x}_1) + \mathbf{n})$ // LR condition
 - 6: Compute $\mathbf{x}_0 = \sqrt{1 - \sigma_p^2} \mathbf{x}_{\text{LR}} + \sigma_p \mathbf{n}_p$
 - 7: Compute $\mathcal{L}_{\text{distill}}$ with Eq. (12)
 - 8: Compute $\mathcal{L}_{\text{align}}$ with Eq. (13)
 - 9: Compute \mathcal{L}_{BC} with Eq. (14)
 - 10: Compute $\mathcal{L}(\phi) = \mathcal{L}_{\text{distill}}(\phi) + \lambda_{\text{align}} \mathcal{L}_{\text{align}}(\phi) + \lambda_{\text{BC}} \mathcal{L}_{\text{BC}}(\phi)$
 - 11: Optimize ϕ with an gradient-based optimizer using $\nabla_\phi \mathcal{L}$
 - 12: **until** $\mathcal{L}(\phi)$ converges
 - 13: **Return** one-step flow \mathbf{v}_ϕ
-

3.4. Comparison to Related Works

In this section, we distinguish the proposed OFTSR from several closely related methods.

BOOT [17]. Gu *et al.* proposed to make the prediction of the student model fulfill the Signal-ODE. In contrast, OFTSR directly constrains the student’s implicit prediction \mathbf{x}_t using the PF-ODE of the teacher model. Moreover, while BOOT was originally designed for text-to-image generation using diffusion models, our method is built on rectified flow and demonstrates a smaller distillation gap compared to BOOT loss for SR task.

DAVI [26]. Lee *et al.* introduced DAVI, which combines Variational Score Distillation (VSD) loss [36, 64, 70] with data consistency loss to train a one-step SR model and utilizes the perturbation trick to present robust restoration ability. However, DAVI needs to train a fake score to track the denoising score of the one-step generator, resulting in reduced training efficiency.

SinSR [63]. Wang *et al.* proposed SinSR, which achieves near-teacher performance by distilling ResShift [74] without adversarial training. However, SinSR requires simulation of the teacher model’s ODE trajectory, leading to computational overhead during training.

Our OFTSR stands out from other diffusion and flow-based SR methods due to its unique ability to restore images with either high perceptual quality or low distortion. This capability is novel among diffusion and flow-based approaches.

4. Experiments

In this section, we provide experimental details and empirical evaluation of OFTSR and compare it with prior works.

4.1. Experimental Setup

Datasets. We perform extensive super resolution experiments on the FFHQ 256×256 [21], DIV2K [1] and ImageNet 256×256 [46] datasets to assess the performance of OFTSR on faces and natural images. For each dataset, we evaluate on 100 hold-out validation images without cheery-picking.

Evaluation Metrics. The metrics we use for comparison are Peak Signal-to-Noise Ratio (PSNR), Fréchet Inception Distance (FID), and Learned Perceptual Image Patch Similarity (LPIPS) [75] distance. The FID evaluates the visual quality by calculating the feature distance between two image distributions. In our experiments, we calculate the FID using the HR images and the restored images from the 100 hold-out validation set with Clean-FID [41]. LPIPS measures the average perceptual similarity between the restored images and their corresponding HR images. PSNR measures the restoration faithfulness between two images. And LPIPS and PSNR are the two main metrics we use to measure the perceptual-fidelity trade-offs.

Compared Methods. We conduct comprehensive comparisons against state-of-the-art diffusion-based image super-resolution methods, which can be categorized into two groups: (1) Training-free methods, including DPS [9], DDRM [22], DDNM [62], DiffPIR [76], CDDB [10], and SITCOM [2]; (2) Training-based methods: GOUB [72], ECDB [73], InDI [11], DAVI [26], I2SB [30], DDC [6], ResShift [74] and SinSR [63]. It is noteworthy that SIT-

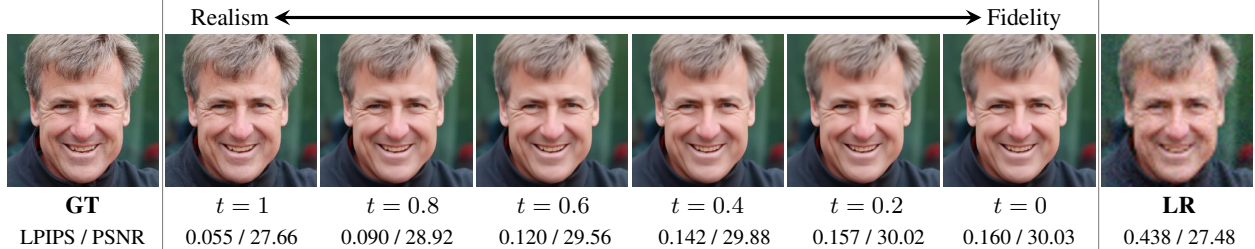


Figure 4. OFTSR is capable to generate continuous transitions between image realism and fidelity.

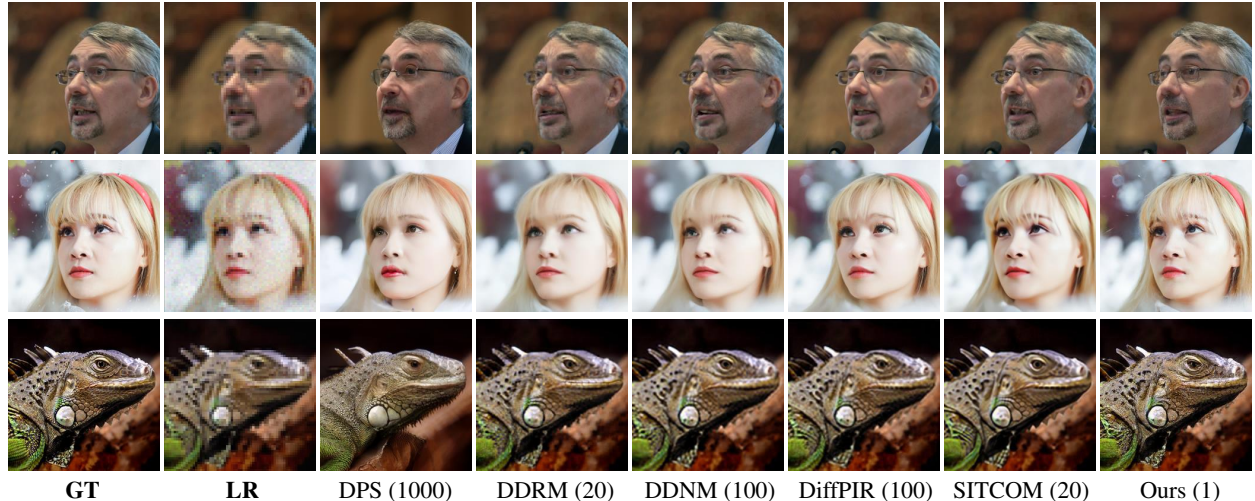


Figure 5. **Qualitative comparison with training-free methods.** The first row shows noiseless SR on the FFHQ dataset, the second row presents noisy SR ($\sigma_n = 0.05$) on FFHQ, and the bottom row demonstrates noiseless SR on the ImageNet dataset. Numbers next to the method names represent the required NFEs.

COM requires K inner-iterations to evaluate and differentiate the score function at each sampling step.

Training Details. We do experiments for both noisy and noiseless SR. For noiseless SR, bicubic downsampling is performed on all three datasets. For noisy SR, we conduct experiment only on FFHQ 256×256 dataset with average-pooling downsampling and Gaussian noise with a standard deviation $\sigma_y = 0.05$. All images are normalized to the range of $[-1, 1]$. For experiments on FFHQ 256×256 and DIV2K, we adopt the same model architecture used for FFHQ in [9]; and for experiment on ImageNet 256×256 , we use the same model architecture as the pretrained unconditional model used in [13]. We modify the input convolution layer to accept concatenated image input. The first stage models are trained from scratch and are sampled with RK45 sampler by default. At the distillation stage, the one-step model is initialized from the teacher model. We use the Adam optimizer with a linear warmup schedule over 1k training steps, followed by a learning rate of $1e-4$ for both stages.

4.2. Results

Quantitative Results. We present comprehensive quantitative evaluations on three benchmark datasets: DIV2K,

| DIV2K | Method | NFEs (\downarrow) | PSNR (\uparrow) | LPIPS (\downarrow) | FID (\downarrow) |
|----------------------------|------------------------------|-----------------------|---------------------|------------------------|----------------------|
| Training-free | DPS [9] | 1000 | 23.05 | 0.447 | 109.35 |
| | DDRM [22] | 20 | 27.87 | 0.285 | 23.38 |
| | DDNM [62] | 100 | 28.09 | 0.279 | 20.33 |
| | DiffPIR [76] | 100 | 27.94 | 0.248 | 19.56 |
| Training-based | IRSDE [37] | 100 | 26.83 | 0.144 | 14.69 |
| | Goub [72] | 100 | 26.92 | 0.218 | 21.56 |
| | ECDB [73] | 100 | 27.39 | 0.212 | 18.88 |
| | InDI [11] | 100 | 26.45 | 0.136 | 15.39 |
| | Ours | 31 | 26.76 | 0.128 | 14.10 |
| | Ours distilled ($t = 1$) | 1 | 26.87 | 0.127 | 14.58 |
| | Ours distilled ($t = 0.5$) | 1 | 28.02 | 0.208 | 16.89 |
| Ours distilled ($t = 0$) | 1 | 28.99 | 0.271 | 18.07 | |

Table 1. Noiseless quantitative results on DIV2K. We compute the average PSNR (dB), LPIPS and FID of different methods on $4 \times$ SR. The best and second best results are highlighted in **bold** and underline.

FFHQ, and ImageNet (Tabs. 1 to 3). Our analysis reveals several findings: (i) The first-stage OFTSR achieves superior performance in perceptual metrics (FID and LPIPS) while requiring fewer than 32 NFEs. (ii) Our distilled version of OFTSR demonstrates remarkable versatility, achieving either the highest PSNR scores or ranking among the top two methods for FID and LPIPS metrics in one step. This indicates minimal performance degradation between the teacher and student models. (iii) Our experiments suggest that FID serves as a more reliable indicator of per-

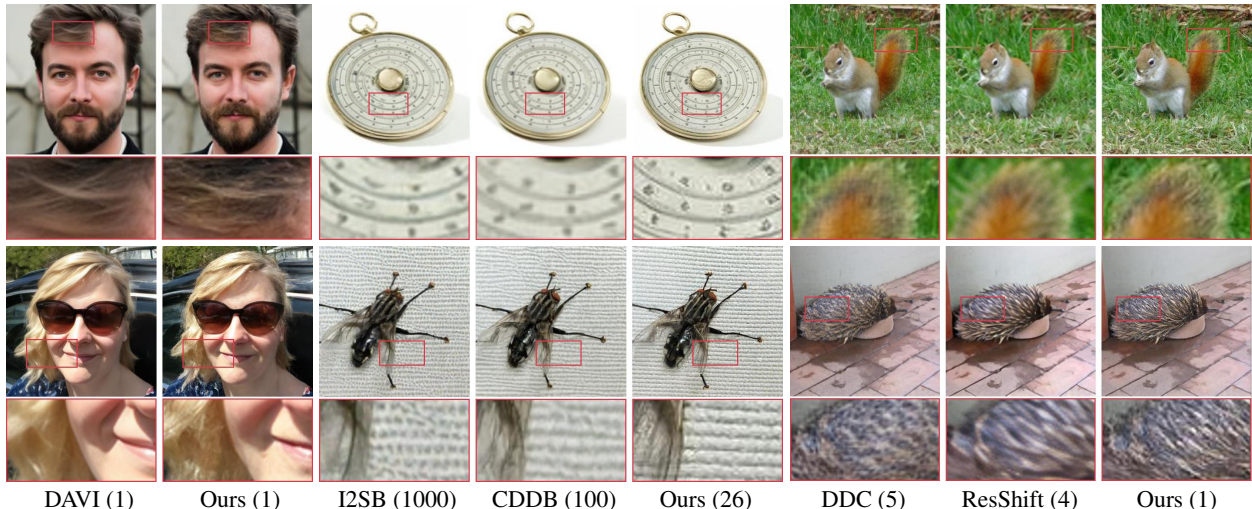


Figure 6. **Qualitative comparison with training-based methods.** The first two columns demonstrate $4\times$ SR results on the FFHQ dataset with noise level $\sigma_n = 0.05$. The remaining columns show noiseless $4\times$ SR results on the ImageNet dataset. Numbers next to the method names represent the required NFEs.

| FFHQ | Method | NFEs (\downarrow) | PSNR (\uparrow) | LPIPS (\downarrow) | FID (\downarrow) | |
|----------------|------------------------------|------------------------------|---------------------|------------------------|----------------------|--------------|
| $\sigma_n = 0$ | Training-free | DPS [9] | 1000 | 24.08 | 0.180 | 79.71 |
| | | DDRM [22] | 20 | 28.81 | 0.118 | 89.12 |
| | | DDNM [62] | 100 | 29.45 | 0.091 | 60.99 |
| | | DiffPIR [76] | 100 | 29.13 | 0.073 | 44.49 |
| | | SITCOM [2] | 20 | 29.29 | 0.089 | 43.00 |
| | Training-based | Ours | 20 | 28.83 | 0.053 | 30.54 |
| | | Ours distilled ($t = 1$) | 1 | 28.98 | <u>0.055</u> | <u>36.02</u> |
| | | Ours distilled ($t = 0.5$) | 1 | <u>29.95</u> | 0.093 | 49.08 |
| | | Ours distilled ($t = 0$) | 1 | 31.25 | 0.150 | 66.76 |
| | | $\sigma_n = 0.05$ | Training-free | DPS [9] | 1000 | 23.61 |
| DDRM [22] | 20 | | | 26.71 | 0.191 | 113.25 |
| DDNM [62] | 100 | | | 27.66 | 0.174 | 113.26 |
| DiffPIR [76] | 100 | | | 26.99 | 0.123 | 61.66 |
| SITCOM [2] | 20 | | | 27.80 | 0.158 | 83.04 |
| Training-based | DAVI [26] | | 1 | 27.50 | 0.084 | 50.19 |
| | Ours | | 20 | 27.28 | 0.080 | 46.04 |
| | Ours distilled ($t = 1$) | | 1 | 27.71 | <u>0.081</u> | <u>49.81</u> |
| | Ours distilled ($t = 0.5$) | | 1 | <u>29.47</u> | 0.157 | 82.93 |
| | Ours distilled ($t = 0$) | | 1 | 29.75 | 0.172 | 85.89 |

Table 2. Noiseless (top) and noisy (bottom) quantitative results on FFHQ 256×256 . We compute the average PSNR (dB), LPIPS and FID of different methods on $4\times$ SR. The best and second best results are highlighted in **bold** and underline.

ceptual quality and better captures the performance gap between teacher and student models during distillation.

Visual Results. Our experimental results demonstrate that OFTSR achieves high-quality image reconstructions. We evaluate OFTSR against leading training-free methods for $4\times$ SR, as shown in Fig. 5. While DPS can produce sharp reconstructions, it requires 1000 NFEs and often introduces significant distortions. In contrast, OFTSR successfully preserves structural information from low-resolution inputs while reconstructing fine details. Notably, our distilled version of OFTSR requires only one NFE, as other training-free methods suffer from severe error accumulation when using less than 10 NFEs. As illustrated in Fig. 6, we also compare OFTSR against state-of-the-art SR methods that require training. The results show that our approach gener-

| ImageNet | Method | NFEs (\downarrow) | PSNR (\uparrow) | LPIPS (\downarrow) | FID (\downarrow) |
|------------------------------|----------------|-----------------------|---------------------|------------------------|----------------------|
| Training-free | DPS [9] | 1000 | 20.36 | 0.438 | 164.99 |
| | DDRM [22] | 20 | 24.55 | 0.292 | 79.99 |
| | DDNM [62] | 100 | <u>25.19</u> | 0.327 | 84.98 |
| | DiffPIR [76] | 100 | 24.88 | 0.306 | 79.42 |
| | SITCOM [2] | 20 | 24.79 | 0.277 | 61.88 |
| | CDDB [10] | 100 | 23.64 | 0.191 | 58.25 |
| | Training-based | I2SB [30] | 1000 | 23.36 | 0.178 |
| DDC [6] | | 5 | 24.67 | 0.156 | 62.06 |
| ResShift [74] | | 4 | 23.68 | 0.207 | 60.75 |
| SinSR [63] | | 1 | 22.25 | 0.204 | 94.90 |
| Ours | | 26 | 23.35 | 0.132 | 46.88 |
| Ours distilled ($t = 1$) | | 1 | 24.20 | <u>0.135</u> | <u>52.69</u> |
| Ours distilled ($t = 0.5$) | | 1 | 24.85 | 0.176 | 60.69 |
| Ours distilled ($t = 0$) | | 1 | 26.18 | 0.284 | 92.04 |

Table 3. Noiseless quantitative results on ImageNet 256×256 . We compute the average PSNR (dB), LPIPS and FID of different methods on $4\times$ SR. The best and second best results are highlighted in **bold** and underline.

ates patterns with rich, natural details. Furthermore, our distilled model enables flexible control over the fidelity-realism trade-offs in the generated high-resolution images. Fig. 4 demonstrates this capability through examples of noisy $4\times$ SR with varying degrees of realism and fidelity.

4.3. Ablations

Perturbation Strength σ_p . In Tab. 4, we evaluate the design choices in the simple conditional flow training stage. All experiments in this ablation study are conducted under identical training conditions, with performance metrics measured using the RK45 solver. The most critical hyperparameter in this ablation is the strength of the perturbation σ_p . Consistent with previous works, we confirm that perturbation is essential for generating perceptually compelling images from LR inputs. Notably, we discover that increasing perturbation strength does not necessarily improve per-

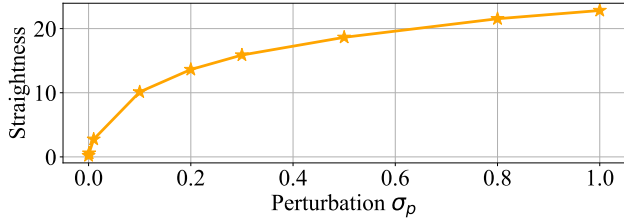


Figure 7. Straightness of conditional flows with different perturbation strength σ_p .

| Strength of Perturbation σ_p | NFEs (\downarrow) | PSNR (\uparrow) | LPIPS (\downarrow) | FID (\downarrow) |
|-------------------------------------|-----------------------|---------------------|------------------------|----------------------|
| 0. | 20 | 29.04 | 0.244 | 110.29 |
| 0.001 | 20 | 29.56 | 0.115 | 48.39 |
| 0.01 | 20 | 29.56 | 0.066 | 34.70 |
| 0.1 | 20 | 28.83 | 0.053 | 30.54 |
| 0.2 | 27 | 28.84 | 0.053 | 30.77 |
| 0.3 | 32 | 28.88 | 0.053 | 31.02 |
| 0.5 | 32 | 28.86 | 0.053 | 30.22 |
| 0.8 | 44 | 28.84 | 0.054 | 31.02 |
| 1. | 44 | 28.82 | 0.053 | 30.75 |
| 0.1 (no cond) | 20 | 28.09 | 0.073 | 42.47 |
| 0.1 (ℓ_2) | 20 | 28.60 | 0.055 | 31.86 |

Table 4. Ablation on noiseless FFHQ 256×256 first stage. The default training setting is $bs = 32$; $lr = 0.0001$; loss type = ℓ_1 ; with condition; all experiments are trained for 100k steps.

ceptual quality but instead leads to more curved PF-ODE, requiring additional NFEs to solve (see Tab. 4). In Fig. 7, we validate this by also measuring the straightness of conditional flows. Furthermore, our experiments demonstrate that conditioning on $\mathbf{x}_{1,R}$ is crucial to compensate for information loss during perturbation. We also find that ℓ_1 loss outperforms ℓ_2 loss for our specific task. While [24] previously highlighted the significance of Gaussian perturbation, our work is the first to systematically analyze the relationship between noise perturbation and the trade-off between generation quality and efficiency in flow-based models.

Distillation Design Space. In Tab. 5, we evaluate several crucial design choices for the distillation stage, including the distillation loss type, solver type, dt value, and the weighting of alignment and boundary losses. Since learning $\mathbf{v}_\phi(\mathbf{x}_{0,LR}, 0)$ is considerably easier than learning $\mathbf{v}_\phi(\mathbf{x}_{0,LR}, 1)$, we utilize metrics from the latter to decide our distillation hyperparameters. Our analysis of the step size dt reveals that smaller values do not necessarily yield better results, leading us to select $dt = 0.05$ for subsequent experiments. Our proposed loss function demonstrates substantial improvement over both the original BOOT [17] loss and PINN [57] distillation loss, achieving a significant LPIPS score improvement of more than 0.1. Further experimentation shows that both the alignment loss (Eq. (13)) and boundary loss (Eq. (14)) contribute to enhanced perfor-

| Distillation Loss | Solver | dt | λ_{align} | λ_{BC} | PSNR (\uparrow) | LPIPS (\downarrow) |
|-------------------|----------|-------|--------------------------|-----------------------|---------------------|------------------------|
| Ours | euler | 0.001 | 0 | 0 | 28.77 | 0.160 |
| Ours | euler | 0.01 | 0 | 0 | 29.35 | 0.076 |
| Ours | euler | 0.02 | 0 | 0 | 29.48 | 0.068 |
| Ours | euler | 0.05 | 0 | 0 | 29.73 | 0.065 |
| Ours | euler | 0.1 | 0 | 0 | 30.05 | 0.073 |
| BOOT [17] | euler | 0.05 | 0 | 0 | 23.81 | 0.483 |
| PINN [57] | euler | 0.05 | 0 | 0 | 27.92 | 0.250 |
| Ours | euler | 0.05 | 0.5 | 0 | 28.19 | 0.234 |
| Ours | euler | 0.05 | 0.2 | 0 | 28.55 | 0.059 |
| Ours | euler | 0.05 | 0.1 | 0 | 29.13 | 0.058 |
| Ours | euler | 0.05 | 0.01 | 0 | 29.65 | 0.064 |
| Ours | euler | 0.05 | 0 | 0.1 | 29.73 | 0.064 |
| Ours | euler | 0.05 | 0.01 | 0.1 | 29.69 | 0.063 |
| Ours | heun | 0.05 | 0.01 | 0.1 | 29.21 | 0.057 |
| Ours | ralston | 0.05 | 0.01 | 0.1 | 29.15 | 0.056 |
| Ours | midpoint | 0.05 | 0.01 | 0.1 | 29.14 | 0.056 |
| Ours (bs=32) | midpoint | 0.05 | 0.01 | 0.1 | 29.07 | 0.055 |

Table 5. Ablation on noiseless FFHQ 256×256 distillation stage. The default training setting is $bs = 8$; $\sigma_p = 0.1$, $lr = 0.0001$; loss type = ℓ_2 ; with LR condition; all experiments are trained for 20k steps; And the one-step metrics are calculated with $t = 1$.

mance. By combining these losses with a midpoint 2-order solver, we achieve additional improvements in our one-step model’s performance at $t = 0$.

5. Limitations and Future Works

While our method advances efficient one-step image super-resolution, we acknowledge several limitations that present opportunities for future research. First, our current approach requires pre-training a conditional flow model as a teacher for the distillation stage. In future work, we plan to explore leveraging strong generative priors, such as Stable Diffusion (SD) [45] and Flux [3], to potentially eliminate this requirement. Second, the performance of our one-step model is inherently constrained by the capabilities of the teacher models. To address this limitation, we propose incorporating supervision from ground-truth high-quality images, either through explicit regression loss or implicit adversarial training. Third, our method currently shows limited robustness to the degradations in low-resolution inputs. Future work will focus on enhancing the model’s ability to handle more complex degradation patterns, thereby improving its practical applicability.

6. Conclusion

In this paper, we introduced OFTSR, a novel approach to developing efficient one-step image super-resolution models. Our extensive experiments on FFHQ, DIV2K, and ImageNet datasets demonstrate that our method significantly improves computational efficiency while maintaining high-quality image restoration capabilities. The proposed framework represents a promising direction in efficient image super-resolution, effectively addressing the perception-distortion trade-off.

References

- [1] Eirikur Agustsson and Radu Timofte. Ntire 2017 challenge on single image super-resolution: Dataset and study. In *Proceedings of the IEEE conference on computer vision and pattern recognition workshops*, pages 126–135, 2017. 2, 5
- [2] Ismail Alkhouri, Shijun Liang, Cheng-Han Huang, Jimmy Dai, Qing Qu, Saiprasad Ravishankar, and Rongrong Wang. Sitcom: Step-wise triple-consistent diffusion sampling for inverse problems. *arXiv preprint arXiv:2410.04479*, 2024. 2, 5, 7
- [3] Black Forest Labs. Flux. <https://blackforestlabs.ai/announcing-black-forest-labs/>, 2024. 8
- [4] Yochai Blau and Tomer Michaeli. The perception-distortion tradeoff. In *Proceedings of the IEEE conference on computer vision and pattern recognition*, pages 6228–6237, 2018. 3
- [5] Tim Brooks, Aleksander Holynski, and Alexei A Efros. Instructpix2pix: Learning to follow image editing instructions. In *Proceedings of the IEEE/CVF Conference on Computer Vision and Pattern Recognition*, pages 18392–18402, 2023. 2
- [6] Hanyu Chen, Zhixiu Hao, and Liying Xiao. Deep data consistency: a fast and robust diffusion model-based solver for inverse problems. *arXiv preprint arXiv:2405.10748*, 2024. 5, 7
- [7] Zheng Chen, Yulun Zhang, Jinjin Gu, Xin Yuan, Linghe Kong, Guihai Chen, and Xiaokang Yang. Image super-resolution with text prompt diffusion. *arXiv preprint arXiv:2311.14282*, 2023. 2
- [8] Jooyoung Choi, Jungbeom Lee, Chaehun Shin, Sungwon Kim, Hyunwoo Kim, and Sungroh Yoon. Perception prioritized training of diffusion models. In *Proceedings of the IEEE/CVF Conference on Computer Vision and Pattern Recognition*, pages 11472–11481, 2022. 2
- [9] Hyungjin Chung, Jeongsol Kim, Michael T Mccann, Marc L Klasky, and Jong Chul Ye. Diffusion posterior sampling for general noisy inverse problems. *arXiv preprint arXiv:2209.14687*, 2022. 2, 5, 6, 7
- [10] Hyungjin Chung, Jeongsol Kim, and Jong Chul Ye. Direct diffusion bridge using data consistency for inverse problems. *Advances in Neural Information Processing Systems*, 36, 2024. 2, 3, 5, 7
- [11] Mauricio Delbracio and Peyman Milanfar. Inversion by direct iteration: An alternative to denoising diffusion for image restoration. *arXiv preprint arXiv:2303.11435*, 2023. 2, 3, 4, 5, 6
- [12] Jia Deng, Wei Dong, Richard Socher, Li-Jia Li, Kai Li, and Li Fei-Fei. Imagenet: A large-scale hierarchical image database. In *2009 IEEE conference on computer vision and pattern recognition*, pages 248–255. Ieee, 2009. 2
- [13] Prafulla Dhariwal and Alexander Nichol. Diffusion models beat gans on image synthesis. *Advances in Neural Information Processing Systems*, 34:8780–8794, 2021. 1, 6
- [14] Laurent Dinh, Jascha Sohl-Dickstein, and Samy Bengio. Density estimation using real nvp. *arXiv preprint arXiv:1605.08803*, 2016. 1
- [15] Patrick Esser, Sumith Kulal, Andreas Blattmann, Rahim Entezari, Jonas Müller, Harry Saini, Yam Levi, Dominik Lorenz, Axel Sauer, Frederic Boesel, et al. Scaling rectified flow transformers for high-resolution image synthesis. In *Forty-first International Conference on Machine Learning*, 2024. 2
- [16] Ian Goodfellow, Jean Pouget-Abadie, Mehdi Mirza, Bing Xu, David Warde-Farley, Sherjil Ozair, Aaron Courville, and Yoshua Bengio. Generative adversarial networks. *Communications of the ACM*, 63(11):139–144, 2020. 1
- [17] Jiatao Gu, Shuangfei Zhai, Yizhe Zhang, Lingjie Liu, and Joshua M Susskind. Boot: Data-free distillation of denoising diffusion models with bootstrapping. In *ICML 2023 Workshop on Structured Probabilistic Inference & Generative Modeling*, 2023. 4, 5, 8, 1
- [18] Amir Hertz, Ron Mokady, Jay Tenenbaum, Kfir Aberman, Yael Pritch, and Daniel Cohen-Or. Prompt-to-prompt image editing with cross attention control. *arXiv preprint arXiv:2208.01626*, 2022. 2
- [19] Jonathan Ho, Ajay Jain, and Pieter Abbeel. Denoising diffusion probabilistic models. *Advances in Neural Information Processing Systems*, 33:6840–6851, 2020. 2, 3
- [20] Aapo Hyvärinen and Peter Dayan. Estimation of non-normalized statistical models by score matching. *Journal of Machine Learning Research*, 6(4), 2005. 2
- [21] Tero Karras, Samuli Laine, and Timo Aila. A style-based generator architecture for generative adversarial networks. In *Proceedings of the IEEE/CVF conference on computer vision and pattern recognition*, pages 4401–4410, 2019. 1, 2, 5
- [22] Bahjat Kawar, Michael Elad, Stefano Ermon, and Jiaming Song. Denoising diffusion restoration models. *arXiv preprint arXiv:2201.11793*, 2022. 2, 5, 6, 7
- [23] Bahjat Kawar, Shiran Zada, Oran Lang, Omer Tov, Huiwen Chang, Tali Dekel, Inbar Mosseri, and Michal Irani. Imagic: Text-based real image editing with diffusion models. In *Proceedings of the IEEE/CVF Conference on Computer Vision and Pattern Recognition*, pages 6007–6017, 2023. 2
- [24] Beomsu Kim, Jaemin Kim, Jeongsol Kim, and Jong Chul Ye. Generalized consistency trajectory models for image manipulation. *arXiv preprint arXiv:2403.12510*, 2024. 3, 8
- [25] Diederik P Kingma and Max Welling. Auto-encoding variational bayes. *arXiv preprint arXiv:1312.6114*, 2013. 2
- [26] Sojin Lee, Dogyun Park, Inho Kong, and Hyunwoo J Kim. Diffusion prior-based amortized variational inference for noisy inverse problems. *arXiv preprint arXiv:2407.16125*, 2024. 2, 3, 4, 5, 7
- [27] Jianze Li, Jiezhong Cao, Zichen Zou, Xiongfei Su, Xin Yuan, Yulun Zhang, Yong Guo, and Xiaokang Yang. Distillation-free one-step diffusion for real-world image super-resolution. *arXiv preprint arXiv:2410.04224*, 2024. 2
- [28] Xinqi Lin, Jingwen He, Ziyang Chen, Zhaoyang Lyu, Bo Dai, Fanghua Yu, Wanli Ouyang, Yu Qiao, and Chao Dong. Diffbir: Towards blind image restoration with generative diffusion prior. *arXiv preprint arXiv:2308.15070*, 2023. 2
- [29] Yaron Lipman, Ricky TQ Chen, Heli Ben-Hamu, Maximilian Nickel, and Matt Le. Flow matching for generative modeling. *arXiv preprint arXiv:2210.02747*, 2022. 2

- [30] Guan-Hong Liu, Arash Vahdat, De-An Huang, Evangelos A Theodorou, Weili Nie, and Anima Anandkumar. I 2 sb: Image-to-image schr\” odinger bridge. *arXiv preprint arXiv:2302.05872*, 2023. 2, 4, 5, 7
- [31] Jiawei Liu, Qiang Wang, Huijie Fan, Yinong Wang, Yandong Tang, and Liangqiong Qu. Residual denoising diffusion models. In *Proceedings of the IEEE/CVF Conference on Computer Vision and Pattern Recognition*, pages 2773–2783, 2024. 2
- [32] Qiang Liu. Rectified flow: A marginal preserving approach to optimal transport. *arXiv preprint arXiv:2209.14577*, 2022. 2, 4
- [33] Ruoshi Liu, Rundi Wu, Basile Van Hoorick, Pavel Tokmakov, Sergey Zakharov, and Carl Vondrick. Zero-1-to-3: Zero-shot one image to 3d object. In *Proceedings of the IEEE/CVF International Conference on Computer Vision*, pages 9298–9309, 2023. 2
- [34] Xingchao Liu, Chengyue Gong, and Qiang Liu. Flow straight and fast: Learning to generate and transfer data with rectified flow. *arXiv preprint arXiv:2209.03003*, 2022. 2, 4
- [35] Eric Luhman and Troy Luhman. Knowledge distillation in iterative generative models for improved sampling speed. *arXiv preprint arXiv:2101.02388*, 2021. 2
- [36] Weijian Luo, Tianyang Hu, Shifeng Zhang, Jiacheng Sun, Zhenguo Li, and Zhihua Zhang. Diff-instruct: A universal approach for transferring knowledge from pre-trained diffusion models. *arXiv preprint arXiv:2305.18455*, 2023. 5
- [37] Ziwei Luo, Fredrik K Gustafsson, Zheng Zhao, Jens Sjölund, and Thomas B Schön. Image restoration with mean-reverting stochastic differential equations. *arXiv preprint arXiv:2301.11699*, 2023. 2, 3, 6
- [38] Morteza Mardani, Jiaming Song, Jan Kautz, and Arash Vahdat. A variational perspective on solving inverse problems with diffusion models. *arXiv preprint arXiv:2305.04391*, 2023. 2
- [39] Fabian Mentzer, George D Toderici, Michael Tschanen, and Eirikur Agustsson. High-fidelity generative image compression. *Advances in Neural Information Processing Systems*, 33:11913–11924, 2020. 2
- [40] Alexander Quinn Nichol and Prafulla Dhariwal. Improved denoising diffusion probabilistic models. In *International Conference on Machine Learning*, pages 8162–8171. PMLR, 2021. 1
- [41] Gaurav Parmar, Richard Zhang, and Jun-Yan Zhu. On aliased resizing and surprising subtleties in gan evaluation. In *Proceedings of the IEEE/CVF Conference on Computer Vision and Pattern Recognition*, pages 11410–11420, 2022. 5
- [42] Ben Poole, Ajay Jain, Jonathan T Barron, and Ben Mildenhall. Dreamfusion: Text-to-3d using 2d diffusion. *arXiv preprint arXiv:2209.14988*, 2022. 2
- [43] Aditya Ramesh, Prafulla Dhariwal, Alex Nichol, Casey Chu, and Mark Chen. Hierarchical text-conditional image generation with clip latents. *arXiv preprint arXiv:2204.06125*, 2022. 1
- [44] Ali Razavi, Aaron Van den Oord, and Oriol Vinyals. Generating diverse high-fidelity images with vq-vae-2. *Advances in neural information processing systems*, 32, 2019. 2
- [45] Robin Rombach, Andreas Blattmann, Dominik Lorenz, Patrick Esser, and Björn Ommer. High-resolution image synthesis with latent diffusion models. In *Proceedings of the IEEE/CVF Conference on Computer Vision and Pattern Recognition*, pages 10684–10695, 2022. 2, 8
- [46] Olga Russakovsky, Jia Deng, Hao Su, Jonathan Krause, Sanjeev Satheesh, Sean Ma, Zhiheng Huang, Andrej Karpathy, Aditya Khosla, Michael Bernstein, et al. Imagenet large scale visual recognition challenge. *International journal of computer vision*, 115(3):211–252, 2015. 5
- [47] Chitwan Saharia, Jonathan Ho, William Chan, Tim Salimans, David J Fleet, and Mohammad Norouzi. Image super-resolution via iterative refinement. *arXiv preprint arXiv:2104.07636*, 2021. 2
- [48] Chitwan Saharia, Jonathan Ho, William Chan, Tim Salimans, David J Fleet, and Mohammad Norouzi. Image super-resolution via iterative refinement. *IEEE transactions on pattern analysis and machine intelligence*, 45(4):4713–4726, 2022. 3
- [49] Tim Salimans and Jonathan Ho. Progressive distillation for fast sampling of diffusion models. *arXiv preprint arXiv:2202.00512*, 2022. 2
- [50] Axel Sauer, Dominik Lorenz, Andreas Blattmann, and Robin Rombach. Adversarial diffusion distillation. In *European Conference on Computer Vision*, pages 87–103. Springer, 2025. 2
- [51] Jascha Sohl-Dickstein, Eric Weiss, Niru Maheswaranathan, and Surya Ganguli. Deep unsupervised learning using nonequilibrium thermodynamics. In *International Conference on Machine Learning*, pages 2256–2265. PMLR, 2015. 2
- [52] Jiaming Song, Arash Vahdat, Morteza Mardani, and Jan Kautz. Pseudoinverse-guided diffusion models for inverse problems. In *International Conference on Learning Representations*, 2023. 2
- [53] Yang Song and Stefano Ermon. Generative modeling by estimating gradients of the data distribution. *Advances in Neural Information Processing Systems*, 32, 2019. 2
- [54] Yang Song, Sahaj Garg, Jiaxin Shi, and Stefano Ermon. Sliced score matching: A scalable approach to density and score estimation. In *Uncertainty in Artificial Intelligence*, pages 574–584. PMLR, 2020. 2
- [55] Yang Song, Jascha Sohl-Dickstein, Diederik P Kingma, Abhishek Kumar, Stefano Ermon, and Ben Poole. Score-based generative modeling through stochastic differential equations. *arXiv preprint arXiv:2011.13456*, 2020. 2, 3
- [56] Yang Song, Prafulla Dhariwal, Mark Chen, and Ilya Sutskever. Consistency models. *arXiv preprint arXiv:2303.01469*, 2023. 2, 4
- [57] Joshua Tian Jin Tee, Kang Zhang, Hee Suk Yoon, Dhananjaya Nagaraja Gowda, Chanwoo Kim, and Chang D Yoo. Physics informed distillation for diffusion models. *Transactions on Machine Learning Research*, 2024. 4, 8, 1
- [58] Chen Wang, Jiatao Gu, Xiaoxiao Long, Yuan Liu, and Lingjie Liu. Geco: Generative image-to-3d within a second. *arXiv preprint arXiv:2405.20327*, 2024. 2
- [59] Haochen Wang, Xiaodan Du, Jiahao Li, Raymond A Yeh, and Greg Shakhnarovich. Score jacobian chaining: Lifting

- pretrained 2d diffusion models for 3d generation. In *Proceedings of the IEEE/CVF Conference on Computer Vision and Pattern Recognition*, pages 12619–12629, 2023. 2
- [60] Jianyi Wang, Zongsheng Yue, Shangchen Zhou, Kelvin CK Chan, and Chen Change Loy. Exploiting diffusion prior for real-world image super-resolution. *International Journal of Computer Vision*, pages 1–21, 2024. 2
- [61] Xintao Wang, Ke Yu, Shixiang Wu, Jinjin Gu, Yihao Liu, Chao Dong, Yu Qiao, and Chen Change Loy. Esrgan: Enhanced super-resolution generative adversarial networks. In *Proceedings of the European conference on computer vision (ECCV) workshops*, pages 0–0, 2018. 3
- [62] Yinhuai Wang, Jiwen Yu, and Jian Zhang. Zero-shot image restoration using denoising diffusion null-space model. *arXiv preprint arXiv:2212.00490*, 2022. 2, 5, 6, 7
- [63] Yufei Wang, Wenhan Yang, Xinyuan Chen, Yaohui Wang, Lanqing Guo, Lap-Pui Chau, Ziwei Liu, Yu Qiao, Alex C Kot, and Bihan Wen. Sinsr: diffusion-based image super-resolution in a single step. In *Proceedings of the IEEE/CVF Conference on Computer Vision and Pattern Recognition*, pages 25796–25805, 2024. 2, 4, 5, 7
- [64] Zhengyi Wang, Cheng Lu, Yikai Wang, Fan Bao, Chongxuan Li, Hang Su, and Jun Zhu. Prolificdreamer: High-fidelity and diverse text-to-3d generation with variational score distillation. *Advances in Neural Information Processing Systems*, 36, 2024. 5
- [65] Lemeng Wu, Chengyue Gong, Xingchao Liu, Mao Ye, and Qiang Liu. Diffusion-based molecule generation with informative prior bridges. *Advances in Neural Information Processing Systems*, 35:36533–36545, 2022. 2
- [66] Rongyuan Wu, Lingchen Sun, Zhiyuan Ma, and Lei Zhang. One-step effective diffusion network for real-world image super-resolution. *arXiv preprint arXiv:2406.08177*, 2024. 2
- [67] Rui Xie, Ying Tai, Chen Zhao, Kai Zhang, Zhenyu Zhang, Jun Zhou, Xiaoqian Ye, Qian Wang, and Jian Yang. Addsr: Accelerating diffusion-based blind super-resolution with adversarial diffusion distillation. *arXiv preprint arXiv:2404.01717*, 2024. 2
- [68] Hanshu Yan, Xingchao Liu, Jiachun Pan, Jun Hao Liew, Qiang Liu, and Jiashi Feng. Perflow: Piecewise rectified flow as universal plug-and-play accelerator. *arXiv preprint arXiv:2405.07510*, 2024. 2
- [69] Tianwei Yin, Michaël Gharbi, Taesung Park, Richard Zhang, Eli Shechtman, Fredo Durand, and William T Freeman. Improved distribution matching distillation for fast image synthesis. *arXiv preprint arXiv:2405.14867*, 2024.
- [70] Tianwei Yin, Michaël Gharbi, Richard Zhang, Eli Shechtman, Fredo Durand, William T Freeman, and Taesung Park. One-step diffusion with distribution matching distillation. In *Proceedings of the IEEE/CVF Conference on Computer Vision and Pattern Recognition*, pages 6613–6623, 2024. 2, 5
- [71] Fanghua Yu, Jinjin Gu, Zheyuan Li, Jinfan Hu, Xiangtao Kong, Xintao Wang, Jingwen He, Yu Qiao, and Chao Dong. Scaling up to excellence: Practicing model scaling for photo-realistic image restoration in the wild. In *Proceedings of the IEEE/CVF Conference on Computer Vision and Pattern Recognition*, pages 25669–25680, 2024. 2
- [72] Conghan Yue, Zhengwei Peng, Junlong Ma, Shiyao Du, Pengxu Wei, and Dongyu Zhang. Image restoration through generalized ornstein-uhlenbeck bridge. *arXiv preprint arXiv:2312.10299*, 2023. 2, 5, 6
- [73] Conghan Yue, Zhengwei Peng, Junlong Ma, and Dongyu Zhang. Enhanced control for diffusion bridge in image restoration. *arXiv preprint arXiv:2408.16303*, 2024. 5, 6
- [74] Zongsheng Yue, Jianyi Wang, and Chen Change Loy. Resshift: Efficient diffusion model for image super-resolution by residual shifting. *Advances in Neural Information Processing Systems*, 36, 2024. 2, 5, 7
- [75] Richard Zhang, Phillip Isola, Alexei A Efros, Eli Shechtman, and Oliver Wang. The unreasonable effectiveness of deep features as a perceptual metric. In *Proceedings of the IEEE conference on computer vision and pattern recognition*, pages 586–595, 2018. 5
- [76] Yuanzhi Zhu, Kai Zhang, Jingyun Liang, Jiezhang Cao, Bihan Wen, Radu Timofte, and Luc Van Gool. Denoising diffusion models for plug-and-play image restoration. In *Proceedings of the IEEE/CVF Conference on Computer Vision and Pattern Recognition*, pages 1219–1229, 2023. 2, 5, 6, 7

OFTSR: One-Step Flow for Image Super-Resolution with Tunable Fidelity-Realism Trade-offs

Supplementary Material

A. Relevant Derivations to Our Distillation Loss

We provide detailed derivation to our distillation loss used in the paper. By substitute intermediate results \mathbf{x}_s and \mathbf{x}_t from student model Eq. (9) into the ODE induced by teacher model Eq. (11), we have:

$$\begin{aligned} \mathbf{x}_t + s\mathbf{v}_\phi(\mathbf{x}_{0,\text{LR}}, s) &= \mathbf{x}_t + t\mathbf{v}_\phi(\mathbf{x}_{0,\text{LR}}, t) + (s-t)\mathbf{v}_\theta(\mathbf{x}_{t,\text{LR}}, t) \\ \implies s(\mathbf{v}_\phi(\mathbf{x}_{0,\text{LR}}, s) - \mathbf{v}_\phi(\mathbf{x}_{0,\text{LR}}, t)) & \\ &= (t-s)\mathbf{v}_\phi(\mathbf{x}_{0,\text{LR}}, t) + (s-t)\mathbf{v}_\theta(\mathbf{x}_{t,\text{LR}}, t) \\ &= dt(\mathbf{v}_\theta(\mathbf{x}_{t,\text{LR}}, t) - \mathbf{v}_\phi(\mathbf{x}_{0,\text{LR}}, t)). \end{aligned} \quad (16)$$

Start from this constraint that applies to the student model, we can construct distillation loss in different forms. (i) In the same spirit as BOOT [17], we make only $\mathbf{v}_\phi(\mathbf{x}_{0,\text{LR}}, s)$ and this will lead to loss Eq. (15). (ii) If we only detach the teacher output, we will end up with loss similar to PINN based distillation PID proposed in [57]:

$$\begin{aligned} \mathcal{L}_{\text{PINN}}(\phi) &:= \mathbb{E}_{\mathbf{x}_1 \sim p_1, t \sim \mathcal{U}[0,1]} \left[\left\| \left[\frac{s}{dt} \left(\mathbf{v}_\phi(\mathbf{x}_{0,\text{LR}}, s) \right. \right. \right. \right. \\ &\quad \left. \left. \left. - \mathbf{v}_\phi(\mathbf{x}_{0,\text{LR}}, t) \right) + \mathbf{v}_\phi(\mathbf{x}_{0,\text{LR}}, t) \right] - \text{SG}[\mathbf{v}_\theta(\mathbf{x}_{t,\text{LR}}, t)] \right\|_2^2 \right]. \end{aligned} \quad (17)$$

Both Eqs. (15) and (17) are loss variants from Eq. (11), and we did not try other variant given the already-good performance of Eq. (15).

In addition, by considering the intermediate interpolation $\mathbf{x}_t = (1-t)\mathbf{x}_0 + t\mathbf{x}_1$ as a special case of $\mathbf{x}_t = \sigma_t\mathbf{x}_0 + \alpha_t\mathbf{x}_1$ in BOOT [17], we can derive the following distillation loss:

$$\begin{aligned} \mathcal{L}_{\text{BOOT}}(\phi) &:= \mathbb{E}_{\mathbf{x}_1 \sim p_1, t \sim \mathcal{U}[0,1]} \left[\frac{1}{\lambda^2} \left\| \mathbf{x}_\phi(\mathbf{x}_{0,\text{LR}}, s) - \right. \right. \\ &\quad \left. \left. \text{SG} \left[\mathbf{x}_\phi(\mathbf{x}_{0,\text{LR}}, t) + \lambda(\mathbf{x}_\theta(\mathbf{x}_{t,\text{LR}}, t) - \mathbf{x}_\phi(\mathbf{x}_{0,\text{LR}}, t)) \right] \right\|_2^2 \right], \end{aligned} \quad (18)$$

where $\lambda = 1 - \frac{t(1-s)}{s(1-t)}$, $\mathbf{x}_\phi(\mathbf{x}_{0,\text{LR}}, t) = \mathbf{x}_0 + \mathbf{v}_\phi(\mathbf{x}_{0,\text{LR}}, t)$, $\mathbf{x}_\phi(\mathbf{x}_{0,\text{LR}}, s) = \mathbf{x}_0 + \mathbf{v}_\phi(\mathbf{x}_{0,\text{LR}}, s)$, and $\mathbf{x}_\theta(\mathbf{x}_{t,\text{LR}}, t) = \mathbf{x}_t + (1-t)\mathbf{v}_\theta(\mathbf{x}_{t,\text{LR}}, t)$ with $\mathbf{x}_t = \mathbf{x}_0 + t\mathbf{v}_\phi(\mathbf{x}_{0,\text{LR}}, t)$. We compared our proposed loss Eq. (15) with its variant Eq. (17) and Eq. (18) in Tab. 5 and our ablation shows that Eq. (15) works best for SR task.

B. Diffusion and Perception-Distortion Trade-off

In practice, we found that our distilled model is slightly off the perception-distortion frontier of the teacher model, as displayed in Fig. 8. To be specific, the corresponding timestep t shifts a bit but for the same MMSE value the first-stage model and distilled model have very close LPIPS value. This might caused by the error from large step size dt used in practice and we leave this for future investigation.

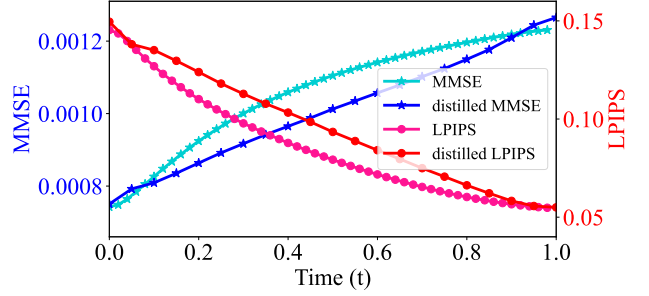


Figure 8. Metrics evaluation of estimated \mathbf{x}_1^t across different timesteps t for both teacher model and distilled one-step model. The teacher model is the same as the one in Fig. 3. We present MMSE instead of PSNR for better visual effect.

C. More Experimental Details

The training of all networks across both stages is smoothed using Exponential Moving Average (EMA) with a ratio of 0.9999. For FFHQ and ImageNet datasets, images are resized to 256 pixels with center cropping, while DIV2K training employs random crops of 256×256 patches. Data augmentation consists of horizontal flips with 50% probability and vertical flips with 6% probability throughout all experiments. For FFHQ noiseless experiment, we use default perturbation std $\sigma_p = 0.1$; for FFHQ noisy experiment, we use a higher perturbation std $\sigma_p = 0.5$ to cover the resized noise from LR images, as suggested in Tab. 6; for both DIV2K and ImageNet we use $\sigma_p = 0.2$. For training, we employed three widely-used datasets: the standard ImageNet training set (1.28M images), the DIV2K training set (800 2K resolution images), and a subset of FFHQ consisting of the first 60,000 images from the dataset. All models are trained until convergence or up to 300k training iterations and we select the model based on best metrics. We train the model with uniform loss weight on t . In the distillation stage, we sample the timestep t using

| σ_p | NFEs (\downarrow) | PSNR (\uparrow) | LPIPS (\downarrow) |
|------------|-----------------------|---------------------|------------------------|
| 0. | 20 | 25.232386 | 0.318569 |
| 0.1 | 20 | 24.088917 | 0.158119 |
| 0.3 | 32 | 24.143854 | 0.154383 |
| 0.5 | 32 | 24.095301 | 0.154208 |
| 1. | 44 | 24.216015 | 0.153059 |

Table 6. Ablation on FFHQ 256×256 first stage with noisy SR; the default training setting is $bs = 32$; $lr = 0.0001$; loss type = ℓ_1 ; with LR condition.

$t \sim \mathcal{U}[t_{\min}, t_{\max}]$ with $t_{\min} = 0.01$ and $t_{\max} = 0.99$ in practice.

For DIV2K evaluation, we first segment the large 2K resolution images into 256×256 patches for model inference, then reconstruct the final image by combining the restored patches. To ensure fair comparison, all generated SR images are stored in a dedicated separated folder with consistent file names across all evaluated methods, followed by metric calculation against the HR folder using our evaluation script. LPIPS scores are computed using the ‘alex’ model architecture. All experiments are conducted using 4 NVIDIA H800 GPUs.

The straightness of the learned flow \mathbf{v} can be calculated with:

$$S(\mathbf{v}) = \int_0^1 \mathbb{E} [\|\mathbf{v}(\mathbf{x}_t, t) - (\mathbf{x}_1 - \mathbf{x}_0)\|^2] dt, \quad (19)$$

We also measured the FID among 50k imagenet validation set and the result FID is 2.458 comparing to 2.8 from I2SB.

D. Additional Experiments

We evaluated our first-stage training on the FFHQ 256×256 dataset using $\sigma_p = 1$ without conditioning, effectively training an unconditional generative model for human faces. For this experiment, we do not use any data augmentation. Our evaluation consists of generating 1k images from random noise using the RK45 sampler (with a ODE tolerance of $1e-3$) and comparing them against the full training dataset of 70k images (we train our unconditional generative flow with the whole dataset). Initial experiments with ℓ_1 loss yielded a FID score of 41.042 with an average of 56 NFEs, which falls short of the previous state-of-the-art P2 model’s score of 28.139 [8]. However, switching to ℓ_2 loss for standard rectified flow training significantly improved performance, achieving a FID of 24.577 with only 44 NFEs on average. The model architecture used in our experiment is the same as the one used in P2. We leave further investigation to this discrepancy between ℓ_1 and ℓ_2 for image generation and

restoration as future works. To facilitate a direct comparison with P2’s best reported results (FID scores of 6.92 and 6.97 with 1,000 and 500 NFEs respectively [8]), we generated 50k samples using our ℓ_2 loss-trained model. Our approach achieved a superior FID score of 5.871 with substantially fewer NFEs (44), demonstrating the effectiveness of rectified flow. Representative non-cherry-picking samples from our model are presented in Fig. 9. As our distillation technique is designed for image restoration tasks, we skip the distillation of this unconditional generation flow.

E. Additional Visual Samples

In this section, we present additional visual results that demonstrate our method’s capabilities. Fig. 10 showcases multiple examples illustrating the tunable fidelity-realism trade-offs achieved on the FFHQ dataset. Figs. 11 and 12 provide comprehensive comparisons between our method and existing approaches on FFHQ and ImageNet images, respectively. Additionally, in Fig. 13, we demonstrate our method’s performance on both real-world SR tasks and AI-generated content enhancement. Results from Figs. 11 to 13 are generated with our distilled one-step model unless otherwise specified.



Figure 9. Random generated samples from unconditional model trained on FFHQ dataset.

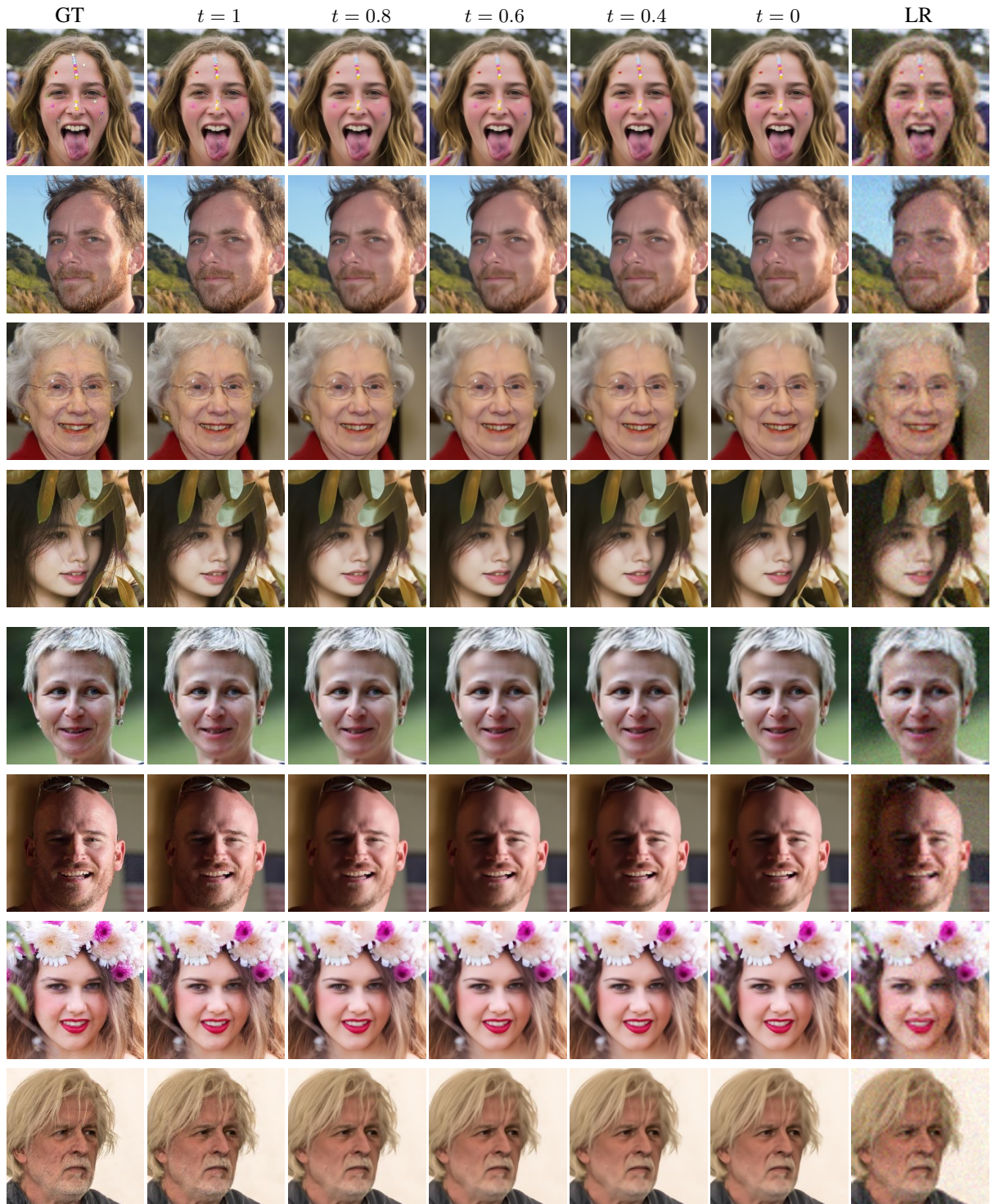


Figure 10. Qualitative results of one-step model with different tunable t .



Figure 11. Qualitative comparisons on FFHQ dataset for $4\times$ SR with $\sigma_n = 0$ (first four rows) and $\sigma_n = 0.05$ (last four rows).

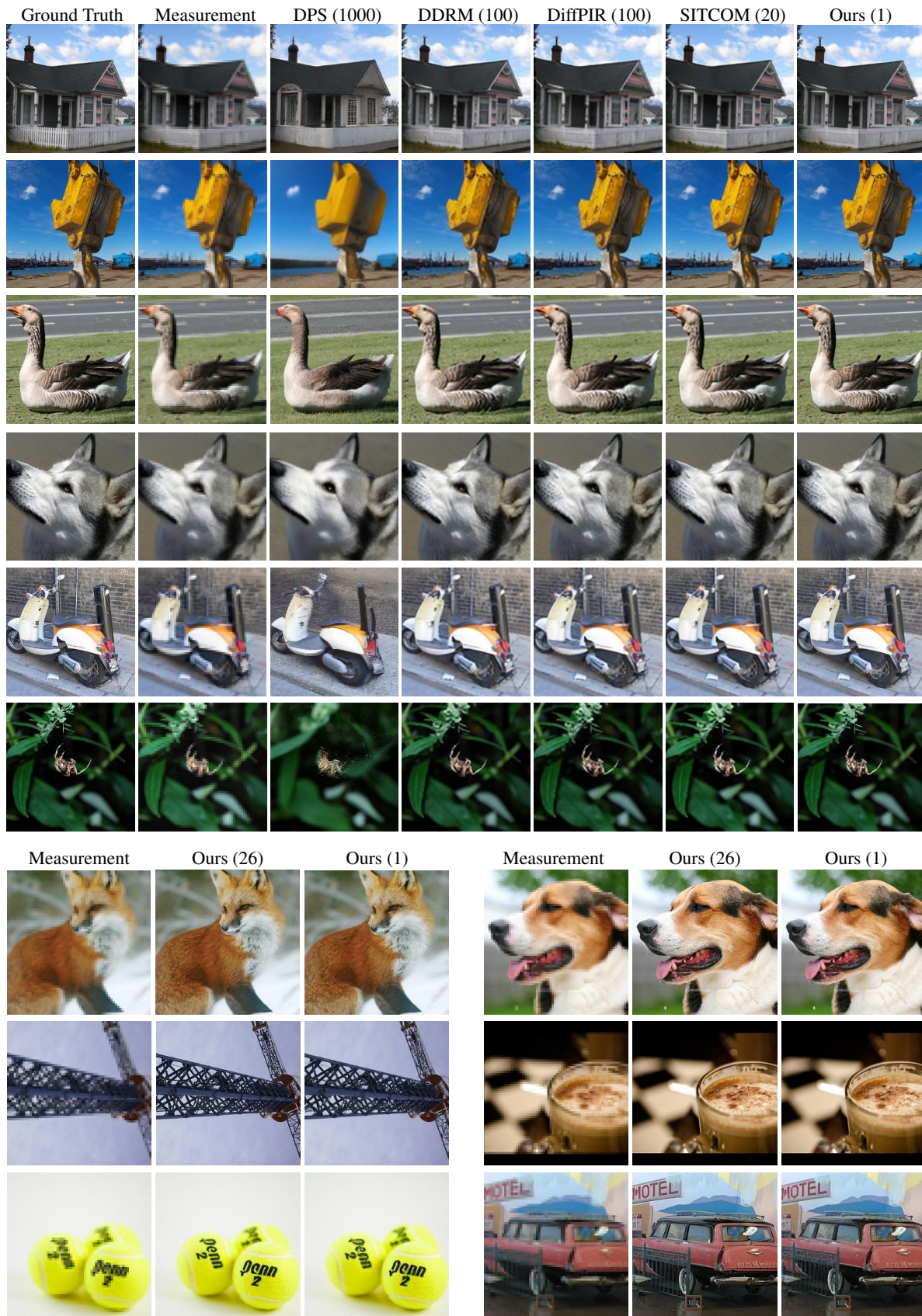


Figure 12. Qualitative comparisons on ImageNet dataset for noiseless $4\times$ SR.

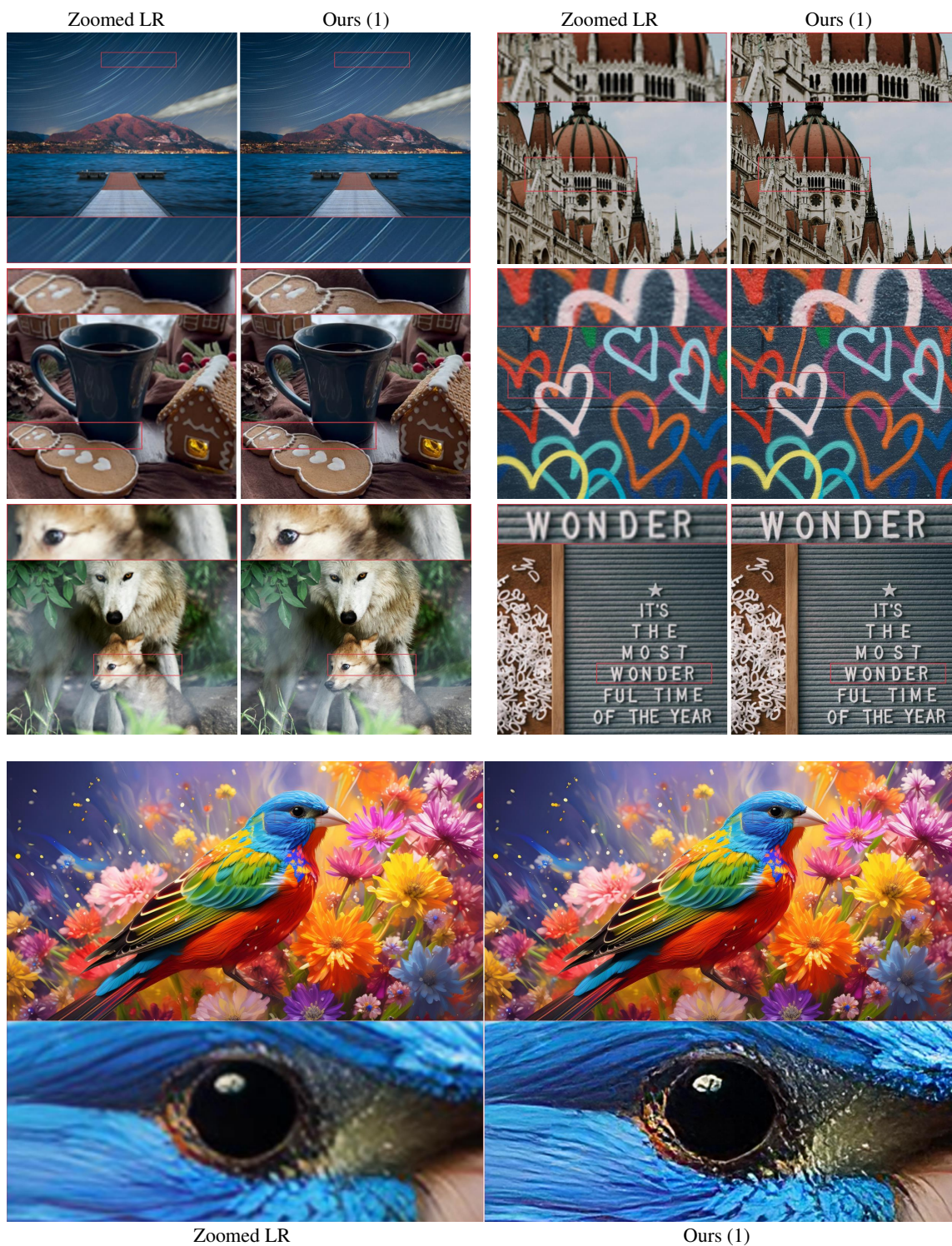


Figure 13. Qualitative results on real data and AI generated content using our 4× SR model trained on DIV2K.